Violation of the Wiedemann-Franz law and ultra-low thermal conductivity of $Ti_3C_2T_x$ MXene

Yubin Huang,[†] Jean Spiece,[†] Tetiana Parker,[‡] Asaph Lee,[‡] Yury Gogotsi,[‡] and Pascal Gehring[*,†]

[†]*Institute of Condensed Matter and Nanosciences, Université catholique de Louvain (UCLouvain), 1348 Louvain-la-Neuve, Belgium*

[‡]*A. J. Drexel Nanomaterials Institute and Department of Materials Science and Engineering, Drexel University, Philadelphia, PA 19104, USA*

E-mail: pascal.gehring@uclouvain.be

Abstract

The high electrical conductivity and good chemical stability of MXenes offer hopes for their use in many applications, such as wearable electronics, energy storage, or electromagnetic interference shielding. While their optical, electronic and electrochemical properties have been widely studied, the information on thermal properties of MXenes is scarce. In this study, we investigate the heat transport properties of $Ti_3C_2T_x$ MXene single flakes using scanning thermal microscopy and find exceptionally low anisotropic thermal conductivities within the $Ti_3C_2T_x$ flakes, leading to an effective thermal conductivity of 0.78 ± 0.21 W m^{-1} K^{-1}. This observation is in stark contrast to the predictions of the Wiedemann-Franz law, as the estimated Lorenz number is only 0.25 of the classical value. Due to the combination of low thermal conductivity and low emissivity of $Ti_3C_2T_x$, the heat loss from it is two orders of magnitude smaller than that

from common metals. Our study explores the heat transport mechanisms of MXenes and highlights a promising approach for developing thermal insulation, two-dimensional thermoelectric, or infrared stealth materials.

Keywords: MXene, thermal transport, thermal conductivity, Wiedemann-Franz law, scanning thermal microscopy.

Introduction

Materials with low thermal conductivity are of utmost importance for a plethora of applications ranging from thermal insulation, to heat shields, and stealth materials, as well as to thermoelectrics.[1] In this context, 2D materials have gained increasing attention since they can possess very low lattice thermal conductivities, because of their two-dimensional crystal structure and phonon-boundary scattering. For example, WSe_2,[2] gallium phosphide (GaP)[3] and indium selenide $(InSe)$[4] reached low values of 0.048 W m^{-1} K^{-1}, 1.52 W m^{-1} K^{-1} and 28.7 W m^{-1} K^{-1}, respectively, which were explained by the strong phonon anharmonicity and boundary scattering. However, these materials often have a low electrical conductivity, making them impractical for use in thermoelectric heat engines. This kind of green energy harvester can generate electricity from the heat with an efficiency proportional to the figure of merit $ZT = \frac{\sigma S^2 T}{\kappa}$, where σ, S and κ are the electrical conductivity, the Seebeck coefficient, and the total thermal conductivity, respectively. Therefore, materials with *low* thermal conductivity and *high* electrical conductivity are desired, a property that is inherently difficult to achieve: in most electrically conductive solids, charge carriers also transport heat. Indeed, the electronic thermal conductivity (κ_e) is related to the electrical conductivity via the Wiedemann-Franz (WF) law. It states that the ratio of κ_e to σ at a given temperature (T) is a constant called the Lorenz number (L_0):

$$L = \frac{\kappa_e}{\sigma T} \equiv L_0 = 2.44 \times 10^{-8} \text{ W}\Omega\text{K}^{-2}. \tag{1}$$

In recent years, it has been experimentally demonstrated that this *fundamental* law can be violated in some materials like graphene,[5] VO_2[6] or in quantum-confined 0D systems.[7] A key ingredient for this violation appears to be strong correlations of quasiparticles, such as strong electron-phonon coupling.[5] To this end, a large family of 2D materials, transition metal carbides and nitrides (MXenes),[8] might be able to demonstrate this violation because some MXenes like $Ti_3C_2T_x$ have a highly tunable metallic-like conductivity of 5000 to over 20000 S cm^{-1}[9] combined with strong electron-phonon interactions.[10–12] However, while their electronic properties have been widely investigated, experimental studies on their thermal transport properties remain lacking, especially on the intrinsic thermal conductivity of isolated single flakes.

In this work, we present local thermal transport measurements on $Ti_3C_2T_x$ MXene single flakes by using scanning thermal microscopy (SThM) at room temperature. By measuring the thermal conductance variation with varying flake thickness, we extracted an ultra-low thermal conductivity of 0.78 W m^{-1} K^{-1}. It coexists with a high electrical conductivity of >4430 S cm^{-1} which leads to a strong violation of the WF law in $Ti_3C_2T_x$ single flakes, with $L = 0.25L_0$. Therefore, our work demonstrates that MXenes provide highly promising 2D materials for ultra-thin heat insulation or thermoelectric applications.

Results and discussion

Synthesis and characterization of $Ti_3C_2T_x$ flakes

$Ti_3C_2T_x$ MXene flakes were synthesized following a well-established process,[13] as described in the Methods section. Briefly, we first etched the aluminium layers of the MAX phase (Ti_3AlC_2) in acidic solution, followed by liquid exfoliation to prepare a colloidal suspension of $Ti_3C_2T_x$ flakes in water (see Figure 1a). A detailed structure characterization of $Ti_3C_2T_x$ can be found in our previous work.[14] Raman spectroscopy was also performed on monolayer $Ti_3C_2T_x$. We observed a typical peak at around 203 cm^{-1} (see Figure S1, SI), which
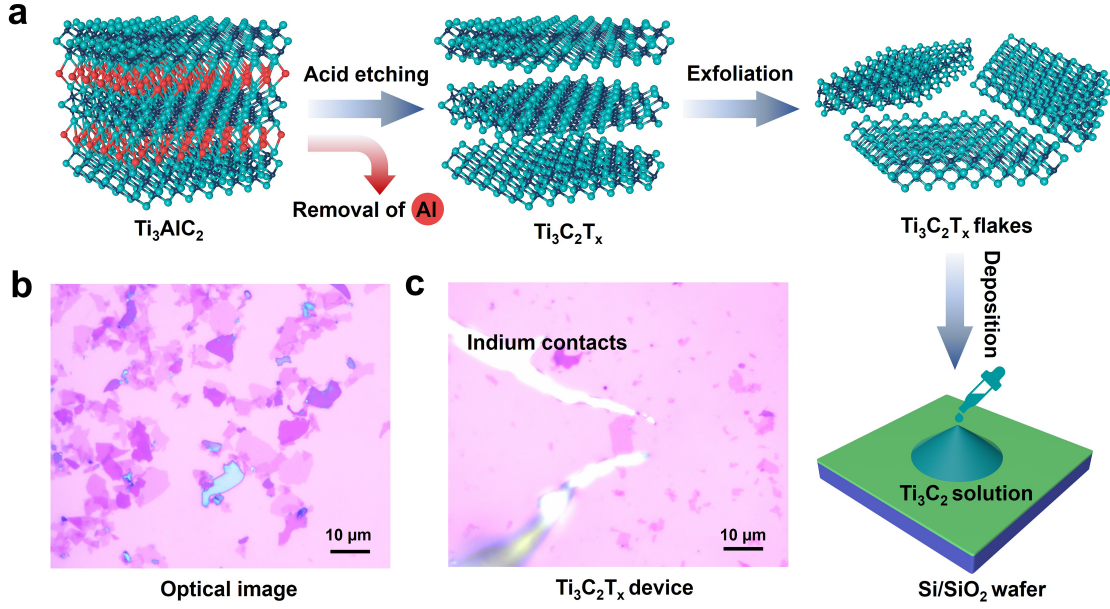
Figure 1: (a) Schematic of the preparation process of $Ti_3C_2T_x$ MXene single flakes and devices. (b) Optical image of monolayer and few-layers $Ti_3C_2T_x$ flakes on SiO_2 substrate. (c) A two-terminal $Ti_3C_2T_x$ device of single flake contacted with two indium needles.

corresponds to out-of-plane vibration mode A_{1g}.[15]

Isolated high-quality $Ti_3C_2T_x$ flakes with lateral sizes of $5\,\mu m$ to $20\,\mu m$ were obtained by drop-casting the dispersion on a Si/SiO_2 wafer (see Experimental methods). Figure 1b shows an optical image of a typical deposit. From their optical contrast (in combination with atomic force microscopy (AFM), Figure 2a), the thickness of $Ti_3C_2T_x$ flakes can be obtained and flakes with thicknesses varying down to the monolayer limit ($\approx 1.8\,nm$, Figure 2e) are identified. For electrical conductance measurements, we fabricated devices by nano-scale soldering of indium[16,17] to the single flakes (Figure 1c).

Thermal transport in $Ti_3C_2T_x$ flakes

To investigate the thermal transport properties of isolated $Ti_3C_2T_x$ flakes with different thicknesses, from monolayer to tens of layers, we used ambient SThM at room temperature ($T_{room} = 293$ K). SThM is a contact mode atomic force microscopy technique in which microfabricated probe is equipped with a Pd electrical resistor on the cantilever and close

to the tip apex (see Figure 2a). This resistor is used as a temperature sensor and local heater, and its resistance is measured using a custom-made Wheatstone bridge.[18,19] Then, the probe is brought into contact with the sample surface. When the mechanical contact occurs, a sharp drop of the probe temperature is observed due to the extra heat transfer opened at the tip apex. Finally, when the tip raster scans the sample surface, the probe temperature is mapped onto the sample topography allowing to calculate the heat flow into the sample and its thermal resistance.
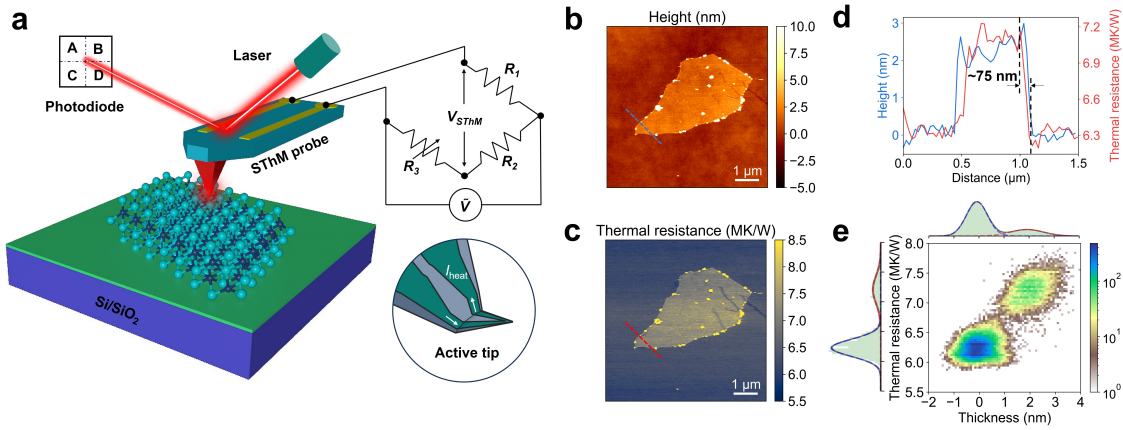

Figure 2: (a) Schematic of the SThM setup for measuring local thermal transport properties of $Ti_3C_2T_x$ flakes. The SThM probe can be used for temperature sensing (with a palladium circuit at the tip apex). Thermal transport signal is measured from Wheatstone bridge output. (b) Topography and (c) thermal resistance maps of monolayer $Ti_3C_2T_x$ on SiO_2 acquired in an ambient environment. (d) Height and thermal resistance curves along the dashed blue line in (b) and red line in (c). Vertical dashed lines are used to estimate the lateral thermal resolution and the tip radius of the SThM probe, which are 38 nm and 75 nm, respectively (see Note S2, SI). (e) 2D histogram showing the relationship between thickness and thermal resistance of the entire image, mean values can be obtained from the Gaussian fit.

Figure 2b and c show a topography and thermal resistance map of a single layer $Ti_3C_2T_x$ flake simultaneously obtained using SThM (single approach-retraction curves which are used for the conversion between the SThM signal and thermal resistance, and details about this conversion are provided in Note S2, SI). We observed a strong thermal resistance contrast between the $Ti_3C_2T_x$ monolayer and the SiO_2 substrate. The thermal resistance increases from 6.3 MK W^{-1} on bare SiO_2 to 7.1 MK W^{-1} on monolayer $Ti_3C_2T_x$ flakes (see Figure

2d). It is worth to note that while such increased thermal resistance can point towards a lower thermal conductivity of $Ti_3C_2T_x$ compared to that of SiO_2, there can be other factors playing a significant role in the apparent thermal transport: i) the thermal contact between the SThM probe and surface can be different for SiO_2 and $Ti_3C_2T_x$; ii) the newly formed interface between the monolayer and SiO_2 substrate can lead to enhanced phonon scattering and thus increased thermal resistance;[20,21] iii) monolayer flake tends to present a thermal barrier, since it's enhanced in-plane thermal spreading is poor when compared to the new interface resistance.[20]

To access the thermal *conductivity* of $Ti_3C_2T_x$, we follow an approach developed in[22–24] that reduces the impact of the effects (i-iii) discussed above. To this end, a model (see Experimental Section and SI) is used to fit the thickness-dependence of the thermal resistance. To extract the relationship between thermal resistance and the thickness of $Ti_3C_2T_x$ flakes, we performed a pixel-to-pixel correlation of height and thermal maps to create 2D histograms (see Figure 2e). This method considers all data points – and does not rely on arbitrarily chosen line-cuts – and we process the data statistically, which reduces experimental errors caused by contaminations or artifacts. For the isolated single-layer case, this histogram shows a two-dimensional Gaussian distribution, and we individually fitted the thickness and thermal resistance with Gaussian functions to obtain their mean values and corresponding standard deviations. For example, the monolayer $Ti_3C_2T_x$ has a thermal resistance of 7.2 $\pm$ 0.23 MK W^{-1}. We applied this method to other SThM data of MXene flakes with different thicknesses (see Figures S4, SI) to create a 2D histogram of all data as shown in Figure 3a. With increasing flake thickness, the thermal resistance increases and approaches the thermal resistance of the bulk $Ti_3C_2T_x$ in the limit of infinite thickness.

Table 1: Extracted fitting parameters through a diffusive thermal transport model

Material	κ_i [W m^{-1} K^{-1}]	κ_c [W m^{-1} K^{-1}]	κ_{eff} [W m^{-1} K^{-1}]	r_{int} [K m^2 W^{-1}]	R_{tip} [K W^{-1}]
$Ti_3C_2T_x/SiO_2$	0.85 to 1.56	0.38 to 0.63	0.78 $\pm$ 0.21	1.0×10^{-8}	3.54×10^6

In the following, we quantify the thermal conductivity of $Ti_3C_2T_x$ using the data in
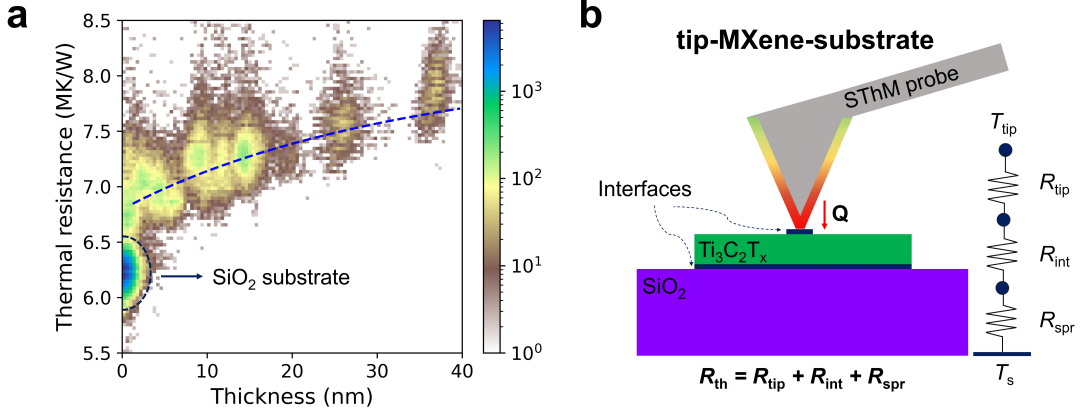
Figure 3: (a) Total 2D histogram combined with all different $Ti_3C_2T_x$ thicknesses and the final fit curve (blue line) through a diffusive thermal transport model to extract thermal properties of $Ti_3C_2T_x$. (b) Schematic of the nanoscopic tip-sample contact and the heat transport model in the tip-MXene-substrate channel used in our experiments.

Figure 3a. We assume a heat transfer mechanism in the tip-MXene substrate channel, which is depicted in Figure 3b. The total thermal resistance measured R_{th} is composed of a series of three resistances $R_{th} = R_{tip} + R_{int} + R_{spr}$, where R_{tip} is the thermal resistance of the tip, R_{int} is the tip-sample interface resistance, and R_{spr} is the thermal spreading resistance. We further assume diffusive heat transport for orthotropic thermal spreading in layered $Ti_3C_2T_x$ flakes, according to previous thermal transport studies on other 2D materials.[25,26] The orthotropic system has thermal conductivities dependent on the direction in the plane (κ_i) and the direction between planes (κ_c). An analytical expression for R_{spr}[21,23,24] was applied to fit the thermal resistance as a function of the thickness of the flake. The resulting fit is shown in Figure 3a as a blue dashed curve, and the fitting parameters are summarized in Table 1. Based on this thermal transport model, we find an interfacial thermal resistance between $Ti_3C_2T_x$ and SiO_2 of r_{int} of 1.0×10^{-8} K m^2 W^{-1}, which is lower than the reported values of interface MoS_2/SiO_2,[27] and close to that of interface graphene/SiO_2.[28] Such a low r_{int} greatly improves the sensitivity and reliability of our SThM measurements.[29] Furthermore, we obtain $\kappa_i = 0.85$ to 1.56 W m^{-1} K^{-1} and $\kappa_c = 0.38$ to 0.63 W m^{-1} K^{-1}, respectively. Thus, the effective thermal conductivity $\kappa_{eff} = 0.78 \pm 0.21$ W m^{-1} K^{-1} is lower than the $\kappa = 1.4$ W m^{-1} K^{-1} of SiO_2, which is consistent with the contrast observed on the SThM
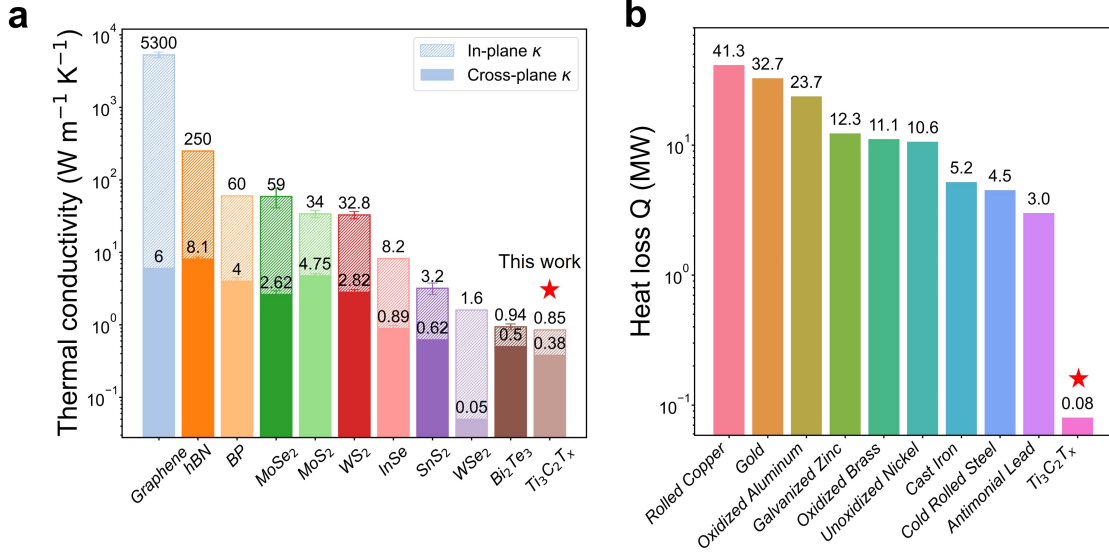
7

maps (see, e.g., Figure 2c).

Figure 4: (a) Comparison of experimental results in thermal conductivity for several 2D materials with monolayers and few layers, including graphene,[30,31] hBN,[32,33] BP,[34] MoSe$_2$,[35,36] MoS$_2$,[36,37] WS$_2$,[36,38] InSe,[4,24] SnS$_2$,[39,40] WSe$_2$,[2,41] Bi$_2$Te$_3$,[42,43] and our work on Ti$_3$C$_2$T$_x$. (b) Comparison of the heat loss for Ti$_3$C$_2$T$_x$ MXene and other common metals in thermal management applications (see Note S5 in SI for detailed calculations).

We further compared the resulting in-/cross-plane thermal conductivities of Ti$_3$C$_2$T$_x$ with other single-crystalline 2D materials with similar thickness, including isolated mono- or few-layer flakes and thin films (Figure 4a). Compared to other 2D materials, Ti$_3$C$_2$T$_x$ shows a record low thermal conductivity, especially in in-plane direction. Surprisingly, this thermal conductivity is almost one order of magnitude smaller than the value estimated using the WF law, where contributions from phonons are neglected: by using the electrical resistance 3.18 kΩ measured in Figure S5 (See SI), we can estimate an electrical conductivity of $\sigma = 4.43 \times 10^5$ S m^{-1} at room temperature (See Note S4 in SI),[44] which is comparable to literature values reported for Ti$_3$C$_2$T$_x$ single flakes.[45] Here, we used the entire thickness of the flake (measured by AFM) instead of the theoretical value (0.98 nm) in electrical measurement. This is the most conservative estimate possible, and still, we observe the breakdown of the WF law. Using Equation 1 we can estimate $\kappa_{\mathrm{WF}} = 3.17$ W m^{-1} K^{-1}, and thus an effective Lorenz number of $L = 0.25L_0$. This strong violation of the WF law

8

will be discussed in the following section. The low thermal conductivity found in $Ti_3C_2T_x$ makes the material attractive for thermal insulation or infrared stealth applications, and we compared its thermal insulation performance (heat loss) with other common metals in thermal management applications (Figure 4b). The heat loss of $Ti_3C_2T_x$ is two orders of magnitude smaller than common metals, such as gold, aluminium and steel, which shows great potential for use as a good thermal barrier in electronic devices and a large variety of other applications. Replacing polished metal casing of industrial equipment with $Ti_3C_2T_x$ foil or use of a submicrometer MXene coating on equipment may save billions of dollars in heat losses.

Discussion

The thermal conductivity of a material contains contributions from electrons (κ_e) and phonons (κ_{ph}): $\kappa_{eff} = \kappa_e + \kappa_{ph}$. Since $Ti_3C_2T_x$ displays a metallic nature with a high density of electronic states near the Fermi level, we can assume that the total thermal conductivity is dominated by electron contributions $(\kappa_e = \kappa_{eff} = 0.78 \ W \ m^{-1} \ K^{-1})$, and that the WF should therefore be valid. However, the observed $L = 0.25L_0$ suggests a strong violation of the WF law. The WF law is a consequence of Fermi liquid theory and has been verified in numerous metals, such as gold or copper, where transport can be successfully described by weakly interacting Landau quasiparticles. In recent years, several violations of the WF law have been reported in strongly correlated systems with strong inelastic scattering of quasiparticles, where the Fermi liquid theory breaks down. Such systems involve graphene at the charge neutrality point,[5] or some transition metal compounds.[6]

Usually, IV- and V-group MXenes (especially $Ti_3C_2T_x$) are metallic with high free carrier densities $(\approx 10^{22} \ cm^{-3})$, which drastically enhances interactions between charge carriers and phonons. This was confirmed in recent experimental studies[10–12] that have provided evidence of strong correlations in MXenes. Using ultra-fast spectroscopy techniques, an electron-phonon coupling strength two orders of magnitude greater than that typically found for

9

conventional metal counterparts was measured in $Ti_3C_2T_x$. Such strong electron-phonon coupling was further observed theoretically and experimentally in another MXene, Nb_2C.[46] Furthermore, high photothermal conversion efficiencies[47] and high phonon frequencies[10] were found in $Ti_3C_2T_x$, which also indicate strong electron-phonon coupling.

These strong correlations found in $Ti_3C_2T_x$ might reveal the mechanism responsible for the violation of the WF law observed in our experiments. Electron-phonon coupling is mainly induced by transverse optical (TO) and longitudinal optical (LO) phonon modes via the short-range deformation potential and the long-range Fröhlich interaction, respectively. Previous studies[10,48] indicate strong electron-TO coupling but weak electron-LO coupling in $Ti_3C_2T_x$ with a higher density of states of TO modes. Energetic electrons strongly interact with TO phonons, which introduces an additional energy dissipation pathway. The weak electron-LO coupling suggested the formation of large polarons based on the Fröhlich polaron theory, which increases the effective mass and decreases charge mobility. These behaviors could be attributed to the reduction of κ_e and the breakdown of the WF law. In addition, κ_e and κ_{ph} may potentially be coupled because of the strong electron-phonon interaction. A theoretical calculation[49] predicted the κ_{ph} of $Ti_3C_2T_x$ ranging from 11 W m^{-1} K^{-1} (with the oxygen surface group) to 108 W m^{-1} K^{-1} (with the fluorine surface group). In our experiment, we expected a mixture of three kinds of surface terminations (-F, -OH, =O). The measured thermal conductivity is still much lower than the calculated values, which consider phonon-phonon and boundary scatterings. This suggested that local defects and inelastic electron-phonon scattering processes may result in a large limitation of the phonon heat transport and a further reduction of κ_{ph}. Therefore, we conclude that the ultralow thermal conductivity of $Ti_3C_2T_x$ single flakes is mainly caused by strong electron-phonon interactions.

Conclusion

We experimentally quantified the anisotropic thermal transport properties of isolated single-crystalline $Ti_3C_2T_x$ flakes by combining scanning thermal microscopy at room temperature and a diffusion heat transfer model. An ultralow thermal conductivity of $\kappa_{eff} = 0.78 \pm 0.21$ W m^{-1} K^{-1} was observed. Given the high electrical conductivity of $\sigma = 4.43 \times 10^5$ S m^{-1} found in our samples, we reveal a strong violation of the WF law, with an effective Lorenz number $L = 0.25 L_0$. We attribute this violation to the strong electron-phonon coupling in $Ti_3C_2T_x$, especially the electron-LO scattering combined with local defects or phonon scatterings that reduce the phononic thermal conductivity. These results provide an experimental basis showing that MXenes are very promising materials for future thermoelectric applications thanks to a high electrical conductivity combined with high thermal resistivity. Furthermore, this work highlights the application potential of $Ti_3C_2T_x$ for thermal management or – thanks to its very low infrared emissivity[50] – for thermal barrier coatings.

Experimental Section

Preparation of $Ti_3C_2T_x$ colloid

$Ti_3C_2T_x$ was etched from Carbon Ukraine Ti_3AlC_2 MAX phase. The etchant was prepared by mixing 6 mL deionized water, 2 mL hydrofluoric acid (51 wt.% aq. Thermo Fisher Scientific), and 12 mL hydrochloric acid (38 wt.% aq. Thermo Fisher Scientific). 1 g Ti_3AlC_2 was then etched for 24 hours at 35 °C and 300 rpm for the stir bar. After etching out the Al, the acid was washed out of the multilayer $Ti_3C_2T_x$ through 8 cycles of centrifugation at 3500 rpm for 3 min per cycle. Once the solution was pH neutral, H_2O was added to make a 20 mL solution, and 0.424 g LiCl was added to make a 0.5 M concentration of Li$^+$ ions, which were then intercalated into the $Ti_3C_2T_x$ by mixing for 24 hours at 35 °C and 300 rpm. After intercalation, the monolayer and few-layer MXene flakes were isolated through repeated

centrifugation and skimming, as only the single flakes remained suspended for collection after centrifugation. Centrifugation conditions were 10 min and 3500 rpm to remove LiCl and repeated until supernatant was no longer clear, with subsequent increases in cycle time for single-layer MXene supernatant collection. About 10-12 cycles were performed, and then the predominantly single-layer $Ti_3C_2T_x$ dispersion was concentrated through centrifugation at 10000 rpm for 20 min.

Fabrication of $Ti_3C_2T_x$ devices

Samples of $Ti_3C_2T_x$ isolated flakes were obtained by drop-casting MXene aqueous dispersion onto a Si/SiO_2 (290 nm-thick SiO_2) substrate, followed by washing with slowly flowing deionized water and naturally dried under a flow of nitrogen gas. The wafers were finally put in an oven at 60 °C to completely dry the flakes. Before deposition, the Si/SiO_2 wafer was ultrasonically cleaned in acetone and then deionized water for 10 min to ensure the cleanliness of the surface. We obtained lots of single MXene flakes with different thicknesses within the drop-cast area. The indium needles were fabricated in $Ti_3C_2T_x$ single flake as electrical contact, which can achieve good ohmic contacts. In this technique,[16] the substrate with indium bead was first heated to around 165 °C and the indium melted. Then, a tungsten tip was inserted into the melting pool and slowly pulled out to form a sharp needle, which was finally transferred to MXene flakes to form the contacts.

SThM measurements on $Ti_3C_2T_x$ devices

Measurements were performed by a Bruke Dimension Icon scanning probe microscope platform with a commercial SThM probe (KNT-SThM-2an, Kelvin Nanotechnology) under an ambient environment. The SThM probe has a resistive palladium heater with a resistor of ≈ 350 Ohms at room temperature and a tip radius of ≈ 75 nm (Figure 2d). Similar to our previous work,[21] we first zeroed the Wheatstone bridge and heated the probe by applying an AC voltage of 2 V at a frequency of 91 kHz with a 2 V DC offset. The probe was scanned

over the sample area with contact mode, and the thermal response V_{SThM} was measured with lock-in amplifier (SRS830) pixel by pixel from the unbalanced bridge caused by the local thermal conductance changes of the sample. By monitoring V_{SThM}, we can create a thermal resistance map of the MXene sample. Finally, the amplified signals were recorded by scanning probe microscope controller for data acquisition using commercial software. Topography and thermal maps of $\mathrm{Ti_3C_2T}_x$ devices could be obtained simultaneously.

Diffusive thermal transport model

MXenes are anisotropic materials with directional-dependent thermal conductivities. To transform such an orthotropic system to an effective isotropic thermal conductivity, we consider an effective thermal conductivity defined as $\kappa_{\mathrm{eff}} = \sqrt{\kappa_{\mathrm{i}} \times \kappa_{\mathrm{c}}}$ and an effective thickness defined as $t_{\mathrm{eff}} = t\sqrt{\frac{\kappa_{\mathrm{i}}}{\kappa_{\mathrm{c}}}} + r_{\mathrm{int}}\kappa_{\mathrm{eff}}$ (t is the physical thickness, r_{int} is the thermal interface resistivity). Here, the first term accounts for the anisotropy and the second includes the MXene-$\mathrm{SiO_2}$ interface thermal resistance. Muzychka[51] and Spiece[23] derived an analytical expression for the thermal spreading resistance:

$$R_{\mathrm{spr}}(t) = \frac{1}{\pi\rho\kappa_{\mathrm{eff}}} \int_0^{\infty} \left[\frac{1 + Ke^{(\frac{-2\xi t_{\mathrm{eff}}}{\rho})}}{1 - Ke^{(\frac{-2\xi t_{\mathrm{eff}}}{\rho})}} \right] J_1(\xi) \sin(\xi) \frac{\mathrm{d}\xi}{\xi^2} \tag{2}$$

Where J_1 is the Bessel function of the first kind of order, ρ is the tip radius, ξ the integration variable, and K is defined as $K = (1 - \frac{\kappa_{\mathrm{sub}}}{\kappa_{\mathrm{eff}}})/(1 + \frac{\kappa_{\mathrm{sub}}}{\kappa_{\mathrm{eff}}})$.

For very thin flakes (less than 10 nm), because the radius of the tip (75 nm) is much larger than flake thickness, the heat dissipation channel from the tip to the substrate is almost vertical (cross-plane direction). With this assumption, we can first use an isotropic thermal model (let $\kappa_{\mathrm{i}} = \kappa_{\mathrm{c}}$) to estimate the cross-plane thermal conductivity κ_{c}. We used this unknown κ_{c} to fit Equation 2 with experimental data (thickness-dependent thermal resistance). In detail, we combined seven 2D histogram maps into one and divided it into multiple small bins. For each column, we selected the bin containing the most data points.

The average value of the data in each bin was then used for fitting. When it reached the best fit, we extracted the value of κ_{c}. Then we used this κ_{c} value to fit thicker flakes, we considered the orthotropic model to calculate the total thermal resistance $R_{\text{th}} = R_{\text{tip}} + R_{\text{int}} + R_{\text{spr}}$ and used the unknown parameters κ_{i}, r_{int} and R_{tip} to fit the experimental data R_{th}. As a result, we obtained the κ_{i}, κ_{c}, r_{int} and R_{tip} values.

Acknowledgement

Supporting Information Available

The following files are available free of charge.

- Raman spectrum of the monolayer $Ti_3C_2T_x$; SThM probe calibration (Probe approach and retraction curves, probe temperature as a function of the supplied power); SEM images of the SThM probe; SThM thermal map on a few layers $Ti_3C_2T_x$; I-V curve of a two-terminal $Ti_3C_2T_x$ device; Thermal management applications of $Ti_3C_2T_x$ (Heat loss model and calculations) (PDF).

References

(1) Qian, X.; Zhou, J.; Chen, G. Phonon-Engineered Extreme Thermal Conductivity Materials. *Nat. Mater.* **2021**, *20*, 1188–1202.

(2) Chiritescu, C.; Cahill, D. G.; Nguyen, N.; Johnson, D.; Bodapati, A.; Keblinski, P.; Zschack, P. Ultralow Thermal Conductivity in Disordered, Layered WSe$_2$ Crystals. *Science* **2007**, *315*, 351–353.

(3) Shen, C.; Hadaeghi, N.; Singh, H. K.; Long, T.; Fan, L.; Qin, G.; Zhang, H. Two-Dimensional Buckling Structure Induces the Ultra-Low Thermal Conductivity: a Comparative Study of the Group GaX (X= N, P, As). *J. Mater. Chem. C* **2022**, *10*, 1436–1444.

(4) Buckley, D.; Kudrynskyi, Z. R.; Balakrishnan, N.; Vincent, T.; Mazumder, D.; Castanon, E.; Kovalyuk, Z. D.; Kolosov, O.; Kazakova, O.; Tzalenchuk, A.; Patanè, A. Anomalous Low Thermal Conductivity of Atomically Thin InSe Probed by Scanning Thermal Microscopy. *Adv. Funct. Mater.* **2021**, *31*, 2008967.

(5) Crossno, J.; Shi, J. K.; Wang, K.; Liu, X.; Harzheim, A.; Lucas, A.; Sachdev, S.; Kim, P.; Taniguchi, T.; Watanabe, K.; Ohki, T. A.; Fong, K. C. Observation of the Dirac Fluid and the Breakdown of the Wiedemann-Franz Law in Graphene. *Science* **2016**, *351*, 1058–1061.

(6) Lee, S.; Hippalgaonkar, K.; Yang, F.; Hong, J.; Ko, C.; Suh, J.; Liu, K.; Wang, K.; Urban, J. J.; Zhang, X.; Dames, C.; Hartnoll, S. A.; Delaire, O.; Wu, J. Anomalously Low Electronic Thermal Conductivity in Metallic Vanadium Dioxide. *Science* **2017**, *355*, 371–374.

(7) Majidi, D.; Josefsson, M.; Kumar, M.; Leijnse, M.; Samuelson, L.; Courtois, H.; Winkelmann, C. B.; Maisi, V. F. Quantum Confinement Suppressing Electronic Heat Flow below the Wiedemann–Franz Law. *Nano Lett.* **2022**, *22*, 630–635.

(8) VahidMohammadi, A.; Rosen, J.; Gogotsi, Y. The World of Two-Dimensional Carbides and Nitrides (MXenes). *Science* **2021**, *372*, eabf1581.

(9) Mathis, T. S.; Maleski, K.; Goad, A.; Sarycheva, A.; Anayee, M.; Foucher, A. C.; Hantanasirisakul, K.; Shuck, C. E.; Stach, E. A.; Gogotsi, Y. Modified MAX Phase Synthesis for Environmentally Stable and Highly Conductive Ti_3C_2 MXene. *ACS Nano* **2021**, *15*, 6420–6429.

(10) Zhang, Q.; Li, J.; Wen, J.; Li, W.; Chen, X.; Zhang, Y.; Sun, J.; Yan, X.; Hu, M.; Wu, G.; Yuan, K.; Guo, H.; Yang, X. Simultaneous Capturing Phonon and Electron Dynamics in MXenes. *Nat. Commun.* **2022**, *13*, 7900.

(11) Guzelturk, B.; Kamysbayev, V.; Wang, D.; Hu, H.; Li, R.; King, S. B.; Reid, A. H.; Lin, M.-F.; Wang, X.; Walko, D. A.; Zhang, X.; Lindenberg, A.; Talapin, D. V. Understanding and Controlling Photothermal Responses in MXenes. *Nano Lett.* **2023**, *23*, 2677–2686.

(12) Colin-Ulloa, E.; Fitzgerald, A.; Montazeri, K.; Mann, J.; Natu, V.; Ngo, K.; Uzarski, J.; Barsoum, M. W.; Titova, L. V. Ultrafast Spectroscopy of Plasmons and Free Carriers in 2D MXenes. *Adv. Mater.* **2023**, *35*, 2208659.

(13) Ghasali, E.; Dizge, N.; Khataee, A.; Alterkaoui, A.; Isik, Z.; Özdemir, S.; Orooji, Y. Biofouling Mitigation of Nb_2AlC and Mo_3AlC_2 MXene-Precursors Doped Polyether Sulfone Mixed Matrix Membranes for Pathogen Microorganisms. *Sci. Total Environ.* **2024**, *929*, 172189.

(14) Han, M.; Shuck, C. E.; Rakhmanov, R.; Parchment, D.; Anasori, B.; Koo, C. M.; Friedman, G.; Gogotsi, Y. Beyond $Ti_3C_2T_x$: MXenes for Electromagnetic Interference Shielding. *ACS Nano* **2020**, *14*, 5008–5016.

(15) Sarycheva, A.; Shanmugasundaram, M.; Krayev, A.; Gogotsi, Y. Tip-Enhanced Raman

Scattering Imaging of Single-to Few-Layer $Ti_3C_2T_x$ MXene. *ACS Nano* **2022**, *16*, 6858–6865.

(16) Girit, Ç. Ö.; Zettl, A. Soldering to a Single Atomic Layer. *Appl. Phys. Lett.* **2007**, *91*, 193512.

(17) Razeghi, M.; Spiece, J.; Oğuz, O.; Pehlivanoğlu, D.; Huang, Y.; Sheraz, A.; Başçı, U.; Dobson, P. S.; Weaver, J. M.; Gehring, P.; Kasırga, T. S. Single-Material MoS_2 Thermoelectric Junction Enabled by Substrate Engineering. *npj 2D Mater. Appl.* **2023**, *7*, 36.

(18) Spiece, J. *Quantitative Mapping of Nanothermal Transport via Scanning Thermal Microscopy*; Springer Theses; Springe/Nature: Switzerland, 2019; pp 1–153.

(19) Spiece, J.; Evangeli, C.; Lulla, K.; Robson, A.; Robinson, B.; Kolosov, O. Improving Accuracy of Nanothermal Measurements via Spatially Distributed Scanning Thermal Microscope Probes. *J. Appl. Phys.* **2018**, *124*, 015101.

(20) Menges, F.; Riel, H.; Stemmer, A.; Dimitrakopoulos, C.; Gotsmann, B. Thermal Transport into Graphene through Nanoscopic Contacts. *Phys. Rev. Lett.* **2013**, *111*, 205901.

(21) Evangeli, C.; Spiece, J.; Sangtarash, S.; Molina-Mendoza, A. J.; Mucientes, M.; Mueller, T.; Lambert, C.; Sadeghi, H.; Kolosov, O. Nanoscale Thermal Transport in 2D Nanostructures from Cryogenic to Room Temperature. *Adv. Electron. Mater.* **2019**, *5*, 1900331.

(22) Spièce, J.; Evangeli, C.; Robson, A. J.; El Sachat, A.; Haenel, L.; Alonso, M. I.; Garriga, M.; Robinson, B. J.; Oehme, M.; Schulze, J.; Alzina, F.; Sotomayor Torres, C.; Kolosov, O. V. Quantifying Thermal Transport in Buried Semiconductor Nanostructures via Cross-Sectional Scanning Thermal Microscopy. *Nanoscale* **2021**, *13*, 10829–10836.

(23) Spiece, J.; Sangtarash, S.; Mucientes, M.; Molina-Mendoza, A. J.; Lulla, K.; Mueller, T.; Kolosov, O.; Sadeghi, H.; Evangeli, C. Low Thermal Conductivity in Franckeite Heterostructures. *Nanoscale* **2022**, *14*, 2593–2598.

(24) Gonzalez-Munoz, S.; Agarwal, K.; Castanon, E. G.; Kudrynskyi, Z. R.; Kovalyuk, Z. D.; Spièce, J.; Kazakova, O.; Patanè, A.; Kolosov, O. V. Direct Measurements of Anisotropic Thermal Transport in γ-InSe Nanolayers via Cross-Sectional Scanning Thermal Microscopy. *Adv. Mater. Interfaces* **2023**, 2300081.

(25) Luo, Z.; Maassen, J.; Deng, Y.; Du, Y.; Garrelts, R. P.; Lundstrom, M. S.; Ye, P. D.; Xu, X. Anisotropic In-Plane Thermal Conductivity Observed in Few-Layer Black Phosphorus. *Nat. Commun.* **2015**, *6*, 8572.

(26) Kim, S. E.; Mujid, F.; Rai, A.; Eriksson, F.; Suh, J.; Poddar, P.; Ray, A.; Park, C.; Fransson, E.; Zhong, Y.; Muller, D. A.; Erhart, P.; Cahill, D. G.; Park, J. Extremely Anisotropic Van der Waals Thermal Conductors. *Nature* **2021**, *597*, 660–665.

(27) Yasaei, P.; Foss, C. J.; Karis, K.; Behranginia, A.; El-Ghandour, A. I.; Fathizadeh, A.; Olivares, J.; Majee, A. K.; Foster, C. D.; Khalili-Araghi, F.; Aksamija, Z.; Salehi-Khojin, A. Interfacial Thermal Transport in Monolayer MoS_2-and Graphene-Based Devices. *Adv. Mater. Interfaces* **2017**, *4*, 1700334.

(28) Chen, Z.; Jang, W.; Bao, W.; Lau, C.; Dames, C. Thermal Contact Resistance between Graphene and Silicon Dioxide. *Appl. Phys. Lett.* **2009**, *95*, 161910.

(29) Pernot, G.; Metjari, A.; Chaynes, H.; Weber, M.; Isaiev, M.; Lacroix, D. Frequency Domain Analysis of 3ω-Scanning Thermal Microscope Probe—Application to Tip/Surface Thermal Interface Measurements in Vacuum Environment. *J. Appl. Phys.* **2021**, *129*, 055105.

(30) Balandin, A. A.; Ghosh, S.; Bao, W.; Calizo, I.; Teweldebrhan, D.; Miao, F.; Lau, C. N. Superior Thermal Conductivity of Single-Layer Graphene. *Nano Lett.* **2008**, *8*, 902–907.

(31) Pop, E.; Varshney, V.; Roy, A. K. Thermal Properties of Graphene: Fundamentals and Applications. *MRS Bull.* **2012**, *37*, 1273–1281.

(32) Jo, I.; Pettes, M. T.; Kim, J.; Watanabe, K.; Taniguchi, T.; Yao, Z.; Shi, L. Thermal Conductivity and Phonon Transport in Suspended Few-Layer Hexagonal Boron Nitride. *Nano Lett.* **2013**, *13*, 550–554.

(33) Jaffe, G. R.; Smith, K. J.; Watanabe, K.; Taniguchi, T.; Lagally, M. G.; Eriksson, M. A.; Brar, V. W. Thickness-Dependent Cross-Plane Thermal Conductivity Measurements of Exfoliated Hexagonal Boron Nitride. *ACS Appl. Mater. Interfaces* **2023**, *15*, 12545–12550.

(34) Jang, H.; Wood, J. D.; Ryder, C. R.; Hersam, M. C.; Cahill, D. G. Anisotropic Thermal Conductivity of Exfoliated Black Phosphorus. *Adv. Mater.* **2015**, *27*, 8017–8022.

(35) Zhang, X.; Sun, D.; Li, Y.; Lee, G.-H.; Cui, X.; Chenet, D.; You, Y.; Heinz, T. F.; Hone, J. C. Measurement of Lateral and Interfacial Thermal Conductivity of Single- and Bilayer MoS_2 and $MoSe_2$ Using Refined Optothermal Raman Technique. *ACS Appl. Mater. Interfaces* **2015**, *7*, 25923–25929.

(36) Jiang, P.; Qian, X.; Gu, X.; Yang, R. Probing Anisotropic Thermal Conductivity of Transition Metal Dichalcogenides MX_2 (M= Mo, W and X= S, Se) Using Time-Domain Thermoreflectance. *Adv. Mater.* **2017**, *29*, 1701068.

(37) Dobusch, L.; Schuler, S.; Perebeinos, V.; Mueller, T. Thermal Light Emission from Monolayer MoS_2. *Adv. Mater.* **2017**, *29*, 1701304.

(38) Sang, Y.; Guo, J.; Chen, H.; Yang, W.; Chen, X.; Liu, F.; Wang, X. Measurement of Thermal Conductivity of Suspended and Supported Single-Layer WS_2 Using Micro-Photoluminescence Spectroscopy. *J. Phys. Chem. C* **2022**, *126*, 6637–6645.

(39) Karak, S.; Bera, J.; Paul, S.; Sahu, S.; Saha, S. Low Thermal Conductivity and Interface Thermal Conductance in SnS_2. *Phys. Rev. B* **2021**, *104*, 195304.

(40) Bai, W.; Hua, Y.; Nan, P.; Dai, S.; Sun, L.; Huang, X.; Yang, J.; Ge, B.; Xiao, C.; Xie, Y. Interlayer Phonon Coupling from Heavy and Light Sublayers in a Natural Van der Waals Superlattice. *J. Am. Chem. Soc.* **2023**, *146*, 892–900.

(41) Mavrokefalos, A.; Nguyen, N. T.; Pettes, M. T.; Johnson, D. C.; Shi, L. In-Plane Thermal Conductivity of Disordered Layered WSe_2 and $(W)_x(WSe_2)_y$ Superlattice Films. *Appl. Phys. Lett.* **2007**, *91*, 171912.

(42) Pettes, M. T.; Maassen, J.; Jo, I.; Lundstrom, M. S.; Shi, L. Effects of Surface Band Bending and Scattering on Thermoelectric Transport in Suspended Bismuth Telluride Nanoplates. *Nano Lett.* **2013**, *13*, 5316–5322.

(43) Teweldebrhan, D.; Goyal, V.; Balandin, A. A. Exfoliation and Characterization of Bismuth Telluride Atomic Quintuples and Quasi-Two-Dimensional Crystals. *Nano Lett.* **2010**, *10*, 1209–1218.

(44) Lipatov, A.; Goad, A.; Loes, M. J.; Vorobeva, N. S.; Abourahma, J.; Gogotsi, Y.; Sinitskii, A. High Electrical Conductivity and Breakdown Current Density of Individual Monolayer $Ti_3C_2T_x$ MXene Flakes. *Matter* **2021**, *4*, 1413–1427.

(45) Lipatov, A.; Bagheri, S.; Sinitskii, A. Metallic Conductivity of $Ti_3C_2T_x$ MXene Confirmed by Temperature-Dependent Electrical Measurements. *ACS Mater. Lett.* **2024**, *6*, 298–307.

(46) Huang, Y.; Zhou, J.; Wang, G.; Sun, Z. Abnormally Strong Electron–Phonon Scattering Induced Unprecedented Reduction in Lattice Thermal Conductivity of Two-Dimensional Nb_2C. *J. Am. Chem. Soc.* **2019**, *141*, 8503–8508.

(47) Wang, C.; Wang, Y.; Jiang, X.; Xu, J.; Huang, W.; Zhang, F.; Liu, J.; Yang, F.; Song, Y.; Ge, Y.; Wu, Q.; Zhang, M.; Chen, H.; Liu, J.; Zhang, H. MXene $Ti_3C_2T_x$: a Promising Photothermal Conversion Material and Application in All-Optical Modulation and All-Optical Information Loading. *Adv. Opt. Mater.* **2019**, *7*, 1900060.

(48) Zheng, W.; Sun, B.; Li, D.; Gali, S. M.; Zhang, H.; Fu, S.; Di Virgilio, L.; Li, Z.; Yang, S.; Zhou, S.; Beljonne, D.; Yu, M.; Feng, X.; Wang, H. I.; Bonn, M. Band Transport by Large Fröhlich Polarons in MXenes. *Nat. Phys.* **2022**, *18*, 544–550.

(49) Gholivand, H.; Fuladi, S.; Hemmat, Z.; Salehi-Khojin, A.; Khalili-Araghi, F. Effect of Surface Termination on the Lattice Thermal Conductivity of Monolayer $Ti_3C_2T_z$ MXenes. *J. Appl. Phys.* **2019**, *126*, 065101.

(50) Han, M.; Zhang, D.; Singh, A.; Hryhorchuk, T.; Shuck, C. E.; Zhang, T.; Bi, L.; McBride, B.; Shenoy, V. B.; Gogotsi, Y. Versatility of Infrared Properties of MXenes. *Mater. Today* **2023**, *64*, 31–39.

(51) Muzychka, Y.; Yovanovich, M.; Culham, J. Thermal Spreading Resistance in Compound and Orthotropic Systems. *J. Thermophys. Heat Transfer* **2004**, *18*, 45–51.

TOC Graphic